

Computational Simulation of Flow Fields for High-speed Aircraft

G. Volpe* and A. Jameson**

**Corporate Research Center, Grumman Corporation, Bethpage, NY 11714 USA*

***Department of Mechanical and Aerospace Engineering, Princeton, NJ 08544 USA*

ABSTRACT

The computation of flow fields about fighter-type aircraft by a new, efficient numerical scheme is discussed. Space discretization is accomplished with a single-block, body-conforming structured mesh. The innovative approach to grid generation can handle very complex configurations with multiple lifting surfaces including aircraft with both horizontal and vertical tails. The time-dependent discretized Euler equations are integrated to steady state via a Runge-Kutta scheme with a local time step. Residual smoothing, enthalpy damping, and a multigrid sequencing of the computational mesh are employed to accelerate convergence. The method, which was designed specifically for transonic applications, can be used efficiently over a wide Mach range covering from low subsonic to supersonic speeds.

INTRODUCTION

The capability of computing aerodynamic flow fields over candidate configurations is of very great value to an aircraft designer. While not replacing the wind tunnel, it complements and, in many ways, it offers considerable timing and economic advantages over the latter. The number of candidate configurations that can be analyzed computationally in a given amount of time is substantially larger than the number that could be examined experimentally due to the long times required for model building and facility scheduling and also due to a relative paucity of experimental facilities. In addition, numerical computations offer the possibility of examining details of the flow that cannot be obtained experimentally.

14 Computers and Experiments in Fluid Flow

Accurate numerical simulations require machines with very large memories and high-speed processors. These are becoming widely available with the advent of supercomputers and minisuper-computers. Even on the machines that are currently in use, however, methods for the solution of the Navier-Stokes equations require running times that are so long as to preclude their frequent use, except in the case of simple geometrical models. In addition, the current status of turbulence modeling lends a measure of unreliability to predictions based on the Navier-Stokes equations. At present, numerical methods based on the Euler equations offer an excellent compromise between reliability, speed, and faithful representation of the flow field.

All numerical methods require a subdivision of the physical space about the configuration that is to be examined. This discretization, or mesh generation, process has matured to the point that meshes about very complex configurations can be generated. The grid generation step can be very complicated, however, and, at times, it can be carried out only by experienced users. It can, in addition, be time-consuming, a feature that may occasionally be unacceptable.

The space about relatively simple shapes can be represented quite well by a single-block structured mesh. In the present context, a structured mesh is one that has a definite topological structure. Single-block meshes are relatively easy to generate. Indeed, the simplest mesh is a Cartesian mesh [1]. Numerical schemes for the solution of partial differential equations work extremely well on such simple meshes. The use of such meshes requires special handling of boundary conditions at the surface of the model. For more complicated shapes (e.g., an aircraft with wings, nacelles, horizontal and vertical tails, etc.), composite meshes made up of several grids separately generated for each individual component would seem more appropriate. In such composite meshes, the individual grids, which may be topologically different, either meet at pre-defined interfaces [2] or overlap [3]. The generation of grids in the latter class is considerably easier than that of grids belonging to the former class. A recently introduced, alternative discretization is provided by unstructured grids [4]. However, methods based on unstructured grids have not yet reached the maturity level of methods based on structured grids. With a mesh that is fine enough to resolve a flow field adequately, the storage requirements and running times of such methods are beyond the capacity of most current computers and the availability of most users. At present, composite grids offer the most versatile approach to the analysis of the flows about complex configurations. Unfortunately, these, too, have drawbacks. First, as mentioned earlier, the grids are not generated

easily. Second, the existence of interfaces or overlaps between the constituent grids requires special treatment of such artificial internal boundaries, inevitably leading to a deterioration of the convergence qualities of the underlying flow-solution scheme and, as a result, longer running times.

In the present work, the development of a method with a relatively simple mesh generation scheme and with a speed of execution high enough to permit its use in a design environment will be described. As will be illustrated, a single-block H-O mesh, which can be easily generated, can be used to represent the space around a large variety of configurations, including rather complex ones. On such a mesh, numerical schemes can be designed to take advantage of the ordered sequence of mesh cells without the encumbrance of internal mesh boundaries. Such a numerical scheme will be described in this paper along with the grid generation process. The basis of the method rests on an algorithm by Jameson [5] for the integration of the time-dependent Euler equations to steady state via a Runge-Kutta scheme. As will be shown, several techniques can be used to accelerate convergence to the steady state.

MESH GENERATION

A single-block H-O mesh about an arbitrary geometrical model can be set up by combining a series of two-dimensional meshes around selected cross sections of the aircraft. Each of these meshes can be generated in planes normal to the longitudinal axis of the aircraft using a conformal mapping technique originally suggested by Moretti [6]. An arbitrary cross section can be mapped into a near circle by removing corners through a sequence of Karman-Trefftz mappings whose number is equal to the number of corners to be removed. In the near-circle plane, a polar-type grid centered on a point equidistant from the vertical extremes of the mapped cross section transforms into a good computational grid in physical space. The circumferential lines of the polar grid are gradually distorted to a perfect circle at a predetermined distance denoting the outer boundary of the mesh.

A typical cross section of the aircraft may cut through one or more components (e.g., fuselage, wing, nacelles, tails), and these may be connected or separated. In the latter case, the separate pieces are connected by slits. If slits are present, care is taken to match up grid points on either side of the slit. By having grid continuity across a slit, application of boundary conditions in the numerical scheme is simplified. The distance to which each 2-D mesh extends is kept constant. Upstream of the aircraft's nose, the first mesh plane on the aircraft is extended to a predetermined distance with gradually increasing spacing between the planes. This portion

16 Computers and Experiments in Fluid Flow

of the grid is purely cylindrical and at its center it contains a degenerate axis. A similar strategy produces a cylindrical grid downstream of the aircraft. This part of the grid wraps around a slit, since the last cross section includes the wing's trailing edge and/or wake. In a typical grid, one-half of the planes are positioned along the aircraft's length and the other half of the planes are divided between the upstream and the downstream portions of the grid.

The grid generated about an F-14-type aircraft (wing, nacelle, horizontal and twin vertical control surfaces) is depicted in Figs. 1 and 2. The wing and both control surfaces have sweptback leading and trailing edges. In Fig. 1 the surface grid is shown reflected about the symmetry plane. The 0 grids around several representative cross sections of the aircraft are shown in Fig. 2. On this configuration, the wake slit coming off the wing is gradually warped to intercept the rearward horizontal tail. As the back end of the aircraft is approached, additional wake slits appear between the engine nacelle and each of the horizontal and vertical tails and the "pancake" between the twin vertical tails. All the slits eventually join to form an "inverted-T" slit extending to infinity.

FINITE VOLUME TIME-STEPPING SCHEME

Discretization of the Euler Equations

An inviscid, rotational flow is described by the Euler equations which are derived from the physical laws of conservation and which embody the notion that, in the absence of singularities, the time rates of change of mass, momentum, and energy contained within any given volume (Ω) must be equal to the net flux of the quantity through the boundary of the volume ($\partial\Omega$). In integral form, the equations can be written as

$$\frac{\partial}{\partial t} \iiint_{\Omega} W^{(m)} d\Omega + \iint_{\partial\Omega} F^{(m)} \cdot dS = 0 \quad (1)$$

Here t is the time, S is the directed surface area, $W^{(m)}$ denotes the five scalar quantities that are conserved, and $F^{(m)}$ is the corresponding vector flux. In a Cartesian coordinate system, the variables and fluxes are given by

$$W^{(1)} = \rho, \quad F^{(1)} = [\rho u, \rho v, \rho w]^T, \quad (2a)$$

$$W^{(2)} = \rho u, \quad F^{(2)} = [\rho u^2 + p, \rho uv, \rho uw]^T, \quad (2b)$$

$$W^{(3)} = \rho v, \quad F^{(3)} = [\rho uv, \rho v^2 + p, \rho vw]^T, \quad (2c)$$

$$W^{(4)} = \rho W, F^{(4)} = [\rho uW, \rho vW, \rho W^2 + p]^T, \quad (2d)$$

$$W^{(5)} = \rho E, F^{(5)} = [\rho Hu, \rho Hv, \rho Hw]^T \quad (2e)$$

where the superscript, T, denotes a transpose operator.

Assuming a perfect gas with a ratio of specific heats equal to γ , the pressure, p , and total enthalpy, H , can be expressed in terms of the density (ρ), the three velocity components (u, v, w), and the total energy (E). Thus,

$$p = (\gamma - 1) \rho \left[E - \frac{1}{2} (u^2 + v^2 + w^2) \right], \quad (3a)$$

$$H = E + \frac{p}{\rho}. \quad (3b)$$

It is assumed that the unknown variables are to be solved for at the nodes of the mesh and that each node (i, j, k) has a control volume consisting of the eight cells meeting at that node. At each node, then

$$\frac{d}{dt} \left(\sum_{n=1}^8 V_n \right) W_n^{(m)} + \sum_{n=1}^8 Q_n^{(m)} = 0 \quad (4)$$

Here, V_n is the volume of the n th cell and $Q_n^{(m)}$ is the net flux through that cell. If the fluxes across the faces of each cell are computed first, then the fluxes through internal faces of the control volume cancel exactly and, therefore, the net flux through each control volume is the sum of the fluxes through the external faces only. Artificial dissipation needs to be added to this scheme in order to prevent the appearance of spurious oscillations that could arise near discontinuities in the solution, such as shocks, or oscillations with an odd-even point mode, which would give a zero net contribution to the flux balance. This artificial dissipation, which goes to zero in the limit of zero mesh spacing, has a low background level everywhere in order to suppress the odd-even point oscillations, and it is increased in the presence of a physical discontinuity in the flow field. The dissipation is constructed in a way that preserves the conservation form of the equations. It is implemented by subtracting from $Q_n^{(m)}$ in Equation (4) a dissipative flux, $D_n^{(m)}$, which is the sum of three terms separately constructed for each of the three computational coordinate directions. For example, the term in the i -coordinate direction is

$$D_{n_i}^{(m)} = r \left[\epsilon^{(2)} - \epsilon^{(4)} \delta_x^2 \right] \delta_x (W_{i+1,j,k}^{(m)} - W_{i,j,k}^{(m)}) \quad (5)$$

where δ_x and δ_x^2 are first- and second-difference operators,

18 Computers and Experiments in Fluid Flow

respectively. $\epsilon^{(2)}$ and $\epsilon^{(4)}$ are adaptive coefficients, and the scaling factor, r , is based on an estimate of the maximum local wave speed. The discontinuities are detected by making $\epsilon^{(2)}$ proportional to a normalized second difference of the pressure. The dissipation terms are of third order, except in regions of steep pressure gradients. The discretization of the convective terms can be shown to be second-order accurate.

Time Integration Assuming the computational mesh to be independent of time, Equation (4) can be rewritten in the form

$$\frac{d}{dt} W_{i,j,k}^{(m)} + R(W^{(m)}) = 0 \quad (6)$$

where $R(W^{(m)})$ denotes the residual. The steady-state solution is obtained by integrating Equation (9) with a multistage Runge-Kutta scheme. If only the steady-state solution is of interest, a locally varying time step, Δt , can be used. With an N -stage scheme, the advance from time (t) to time $(t+\Delta t)$ in each variable W is computed by recursive formulas of the type

$$W^{(n)} = W(t) - \alpha_n \Delta t R(W^{(n-1)}) \quad (7)$$

where $\alpha_0 = 0$ and $W^{(N)} = W(t + \Delta t)$. A five-stage scheme with $\alpha_1 = 1/4$, $\alpha_2 = 1/6$, $\alpha_3 = 3/8$, $\alpha_4 = 1/2$, and $\alpha_5 = 1$ has worked very well in practice. Also, in concert with the findings of Jameson [7], the artificial dissipation terms can be frozen at the values computed during the second stage. This strategy not only decreases the computing time, but also increases the stability margin of the scheme.

Convergence Acceleration

Residual Smoothing As indicated in previous studies [Ref. 5, for example] computational efficiency can be enhanced by a smoothing of the residuals. The maximum permissible time step is set by the local Courant number. This limitation is relaxed if each residual is replaced by an average of its neighbors. This average can be computed implicitly, thus increasing the support of the numerical scheme.

Enthalpy Damping Assuming the flow to be homoenthalpic, convergence to the steady state can be accelerated by enthalpy damping. This technique exploits the difference between the transient value of the locally computed enthalpy and its known, steady-state value, which is also the value at infinity. If one assumes that the rate of change of each variable is proportional to this difference, a new, improved estimate of a variable W can be obtained by adding to the value computed at the end of the Runge-Kutta step the product of the enthalpy discrepancy and a user-defined constant.

Multigrid Strategy The time marching to steady state could be looked at as an iterative process of reducing the errors

(i.e., residuals) at each node. Errors are reduced by an exchange of information between nodes, and, during each iterative cycle, information to any particular node comes only from nodes involved in computing the residual at the node. The exchange of information between two particular points in space takes place faster on coarser grids. It would seem advantageous, then, to devise a strategy that would use this faster approach to the steady state on a coarser grid to generate information that can be used to accelerate the approach to the steady state on any given finer grid. This was the basic idea of multigrid schemes when first presented by Brandt [8]. Here, the scheme described by Jameson [9] is followed.

In the present approach, the coarser mesh is generated by eliminating alternate points in each of the coordinate directions of a given mesh. Then, at each point on a coarse mesh ($K+1$), the values of the variables W at the coincident point on next-higher-level mesh (K) are injected. Once this is accomplished, Runge-Kutta time steps can be performed on the coarse mesh. The time step on the coarse grid is performed with a modified residual, however. The modified residual on the coarser mesh is obtained by adding to the standard, computed residual a term P_{K+1} reflecting the difference between the residual computed on the finer mesh and the residual computed on the coarser mesh using the values transferred from the finer grid. The former is taken to be a weighted average of the residuals at the 27 points nearest the coincident point on mesh level K (including the point itself). In returning to level K , the correction to W calculated on level $K+1$ is used to provide an improved value of the variable on the finer mesh. At coincident points of the two meshes, the improved value is simply the value of W on the coarser mesh. At intermediate points, a trilinearly interpolated value of the difference between values at two mesh levels is added to the current value on the finer mesh. Since on the coarser meshes the time steps are performed in only a fraction of the time needed on the fine mesh, the reduction in the total number of time steps outweighs the cost of sequencing through the grids by a large margin.

BOUNDARY CONDITIONS

At node points lying on the aircraft, flow tangency is enforced at the end of each time step by setting to zero any normal component of velocity. In addition, fluxes through faces lying on the aircraft surface are explicitly set to reflect this condition. Continuity is enforced across wake slits behind the wing by replacing the values of each variable at matching nodes by their average. Similarly, values at nodes sharing a common grid point on the degenerate axis ahead of the aircraft are replaced by the average. At the outer

boundaries of the mesh, appropriate inflow or outflow boundary conditions are imposed using Riemann invariants to attenuate the spurious reflections of outgoing waves into the field. With zero sideslip, in addition, only one-half of the flow field need be considered. In this case, symmetry is enforced on the plane of symmetry of the aircraft.

NUMERICAL EXAMPLES

The first example in Fig. 3 shows surface pressure distributions over selected cross sections of the F-14-type configuration depicted in Figs. 1 and 2. The calculations were performed at a Mach number of 0.80 and an angle of attack of 5 deg. The computational mesh contained a total of 145 half-planes normal to the longitudinal axis of the aircraft. Of these, 97 were on the aircraft itself and the remaining were evenly divided between the regions upstream and downstream of the body. Each half-plane in turn contained 97 points in the circumferential direction and 49 points in the radial direction. In Fig. 3 the four cross sections, whose geometry is depicted in the lower parts of the figure, denote stations along the wing. Evidence of a shock is clearly indicated in the outboard portion of the wing. At these flow conditions, the flow is well-behaved, and nothing unusual is observed.

A more interesting flow is encountered when the configuration is analyzed at an angle of attack of 20 deg. (and the same Mach number). The cross-sectional pressure distributions are shown in Fig. 4, and the Mach number contours on the surface and in a mid-fuselage cross-sectional plane are depicted in Fig. 5. In Fig. 4, there is indication of a shock close to the leading edge of the glove and the wing, and this shock can be discerned as a clustering of contour lines in Fig. 5. This shock apparently causes the flow to separate. Some of the surface pressure distributions depicted in Fig. 4 reveal a definite suction effect (evidenced by the "rounded" patterns around a local pressure minimum). The pattern is typical of flows where a vortex lies over the wing. Additional evidence of flow separation is offered by Fig. 6, which shows entropy contours on the surface and selected planes over the aircraft. Entropy is generated near the wing tip, and the contours order themselves in a definite vortex-like pattern. Figure 7 depicts some streamlines of this flow. The left side of the aircraft, in this head-on view, shows streamlines started near the wing-glove junction, and these streamlines can be seen to wrap into a tight vortex. The right side shows, in addition, the streamlines from the wing's leading edge. This latter set can also be seen to separate and to wrap around the inner vortex.

The numerical method has been used on a wide variety of configurations over a considerable Mach number range, and this

will be illustrated in the next two examples. In Fig. 8 the cross-sectional pressure distributions computed on a generic fighter aircraft at a free-stream Mach number of 0.20 and an angle of attack of 25 deg. are shown. The configuration features a chine-shaped forebody and a sharp-edged, cropped delta wing. A vortex is generated by the chine and another vortex is generated by the wing's leading edge. There is considerable interaction between the two vortices as shown in Fig. 9. The configuration is similar to the one treated by Erickson and Brandon [10], and a sketch of their observations is in good agreement with the computed streamline pattern, as Fig. 9 shows. This computation was carried out on a $97 \times 97 \times 49$ mesh, with one-half of the cross-sectional planes stacked over the aircraft body.

The final example in Fig. 10 depicts the pressure distributions along four meridian lines running along the length of a spherically blunted, biconic missile body at Mach 6 and an angle of attack of 10 deg. This configuration consists of a front and a rear conical section whose half angles are 12.84 and 7 deg., respectively. The body has been tested by Miller and Gnoffo [11] and their experimental measurements also are shown. The agreement between the computations and the experiment is quite good, except in the vicinity of the nose of the missile, a region in which the grid is too coarse to describe the flow adequately. In particular, the shock position is predicted very well. The calculation was performed with a mesh comprising 65 longitudinal planes, of which only eight were located upstream of the nose and eight downstream, because of the restricted domains of dependence and influence in this purely supersonic flow. Each cross-sectional plane contained 49 points in the circumferential direction and 33 in the radial direction.

CONCLUDING REMARKS

The method has proved to be very reliable and efficient in all cases, even those where substantial flow separation is encountered. Convergence to steady state, defined by a reduction in the average residual of a minimum of three orders of magnitude, is typically achieved in 200-300 cycles. The convergence rate of the algorithm for a particular geometry and set of flow conditions has shown very little sensitivity to mesh size. Thus, on refining a particular mesh, the time needed to advance one time step increases linearly with the number of grid points, but the number of time steps needed for convergence is largely unchanged. On the 689,185-point mesh used for the calculations over the F-14-like body each time step required approximately 30 sec. of CPU on a Cray-XMP machine. The speed of the solution algorithm combined with the relative simplicity of the grid generation process, even in cases where bodies of considerable geometric complexity are

22 Computers and Experiments in Fluid Flow

considered, make the method an ideal tool in a preliminary design environment.

REFERENCES

1. Albone, C.M. An approach to geometry and flow complexity using feature associated mesh embedding (FAME): strategy and first results. Numerical Methods for Fluid Dynamics 3, ed.: K.W. Morton and M.J. Baines, 215-235 (1989).
2. Rai, M.M. A relaxation approach to patched-grid calculations with the Euler equations. J. Comp. Phys. **66**, 99-131 (1986).
3. Benek, J.A., Donegan, T.L., and Suhs, N.E. Extended chimera grid embedding scheme with applications to viscous flows. Proc. AIAA 8th Computational Fluid Dynamics Conf., Honolulu, HI, 283-291 (1987).
4. Jameson, A., Baker, T.J., and Weatherill, N. Calculation of inviscid transonic flows over a complete aircraft. AIAA Paper 86-0103, AIAA 24th Aerospace Sciences Meeting, Reno, NV, January 1986.
5. Jameson, A. A vertex-based multigrid algorithm for three-dimensional compressible flow calculations. ASME Symp. on Numerical Methods for Compressible Flow, Anaheim, CA (1986).
6. Moretti, G. Conformal mappings for computations of steady, three-dimensional, supersonic flows. ASME Winter Mtg., New York (1976).
7. Jameson, A. Multigrid algorithm for compressible flow calculations. Second European Conference on Multigrid Methods, Cologne, October, 1985, Princeton University Report MAE 1743.
8. Brandt, A. Multi-level adaptive solution to boundary value problems. Math. Comp. **31**, 333-390 (1977).
9. Jameson, A. Solution of the Euler equations by a multigrid method. Applied Math and Computation **13**, 327-356 (1983).
10. Erickson, G.E., and Brandon, J.M. On the nonlinear aerodynamic and stability characteristics of a generic chine-forebody slender-wing fighter configuration. NASA TM 89447 (1987).

11. Miller, C.G., and Gnoffo, P.A. Pressure distributions and shock shapes for $12.84^\circ/7^\circ$ on-axis and bent-nose biconics in air at Mach 6. NASA TM 53222 (1981).

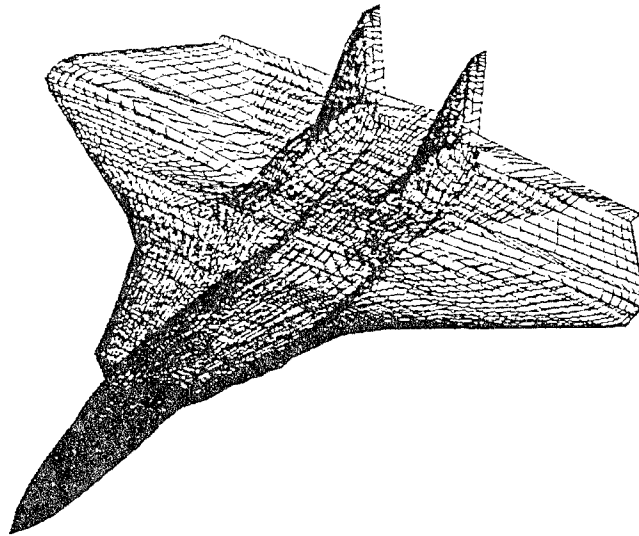


Figure 1: Surface/wake grid on F-14-type aircraft.

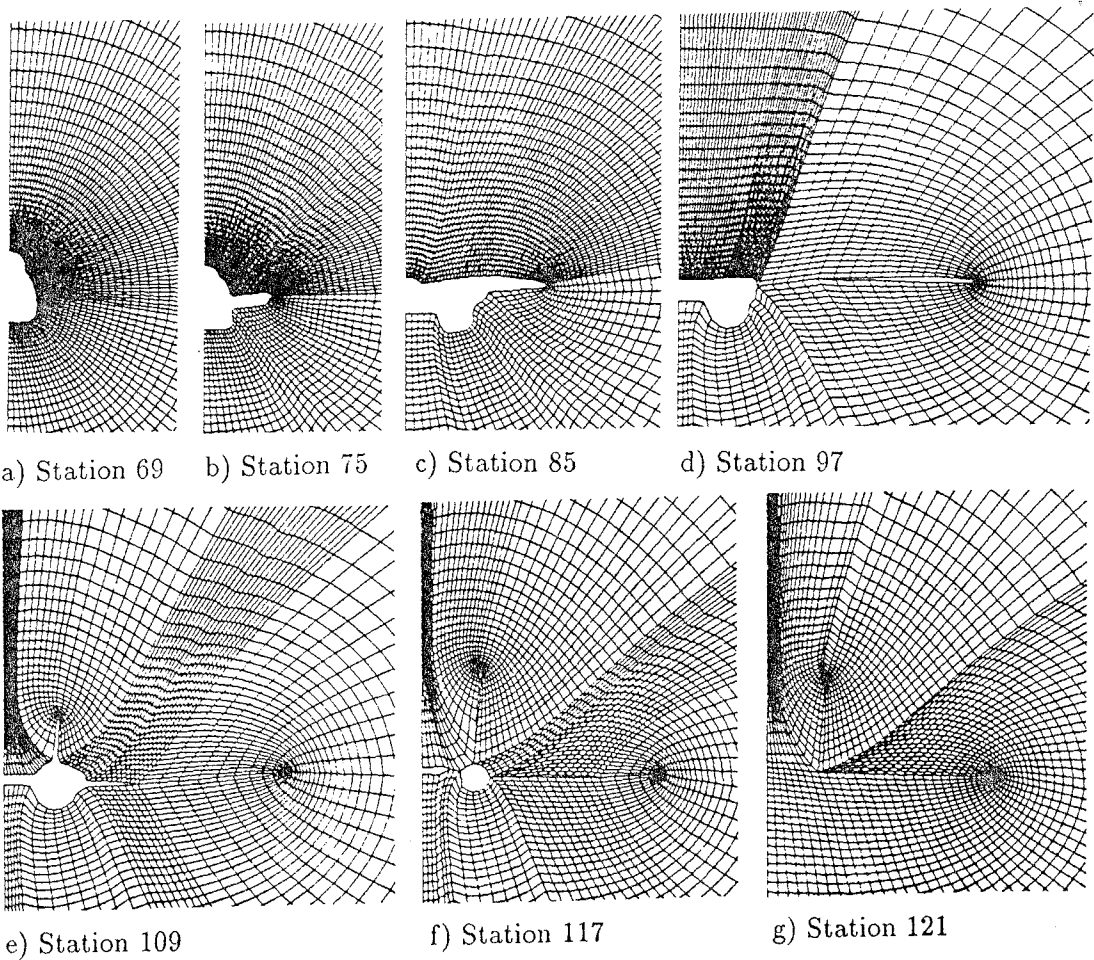


Figure 2: Representative cross-sectional grid planes on F-14-type aircraft.

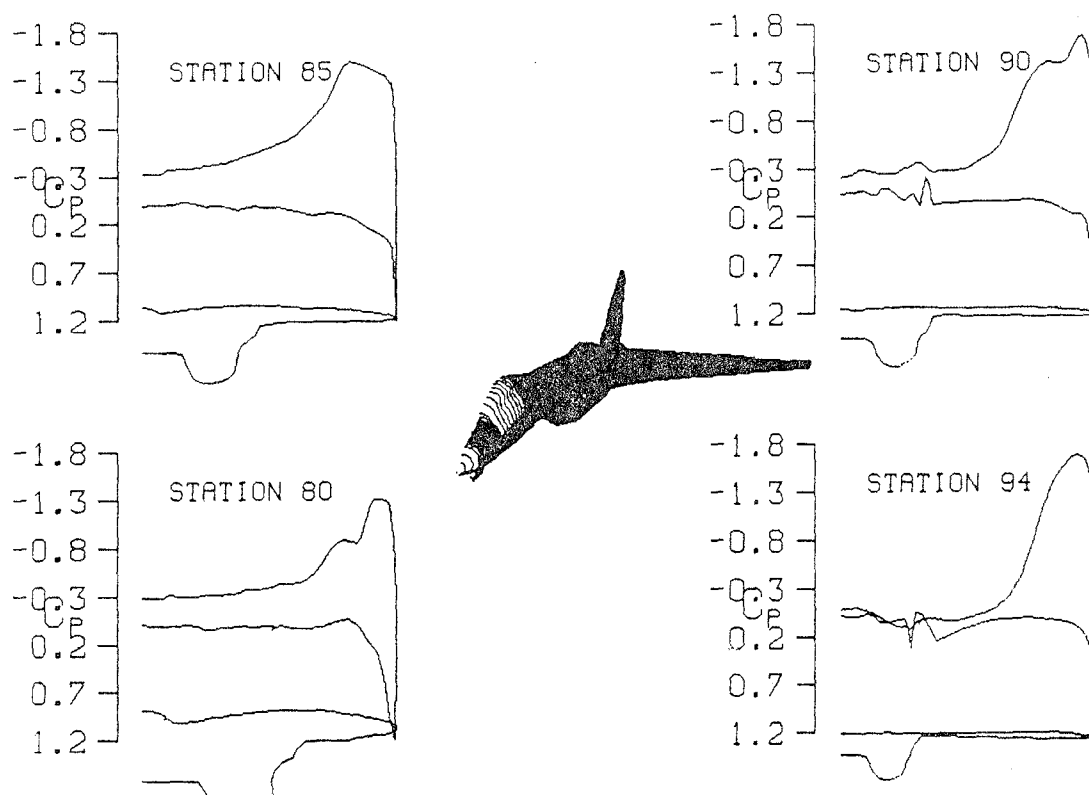


Figure 3: Computed cross-sectional surface pressure distributions on F-14-type aircraft; $M_\infty = 0.80$, $\alpha = 5^\circ$.

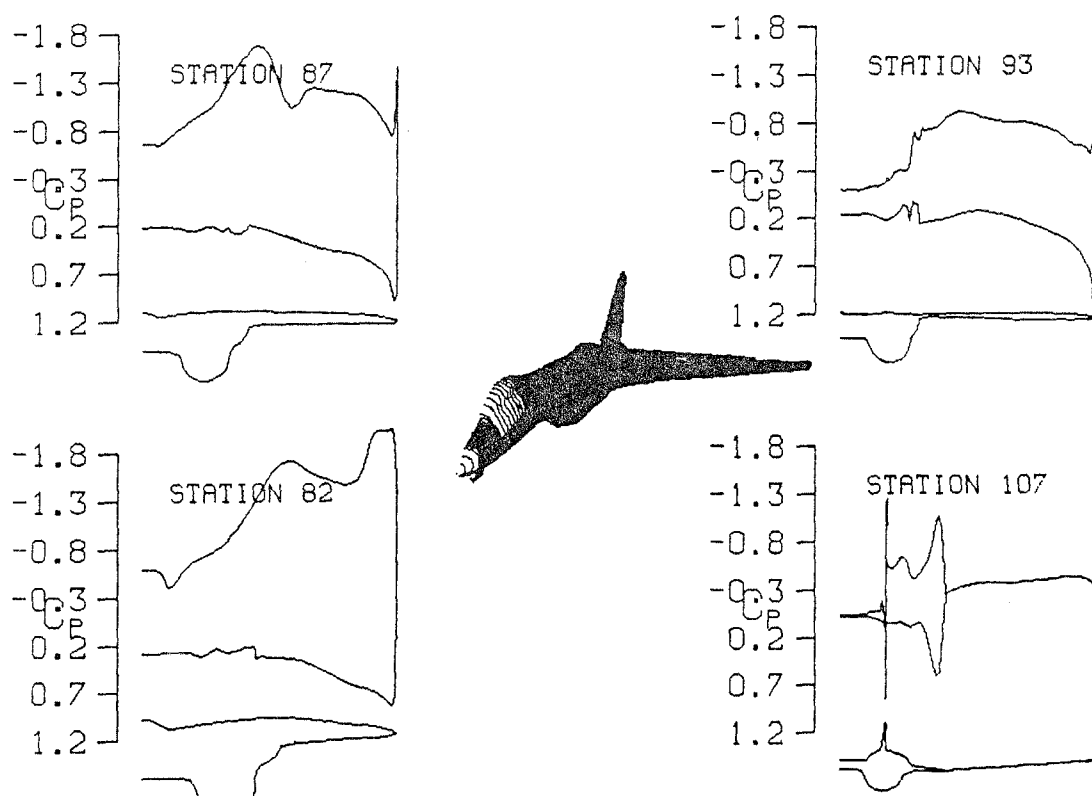


Figure 4: Computed cross-sectional surface pressure distributions on F-14-type aircraft; $M_\infty = 0.80$, $\alpha = 20^\circ$.

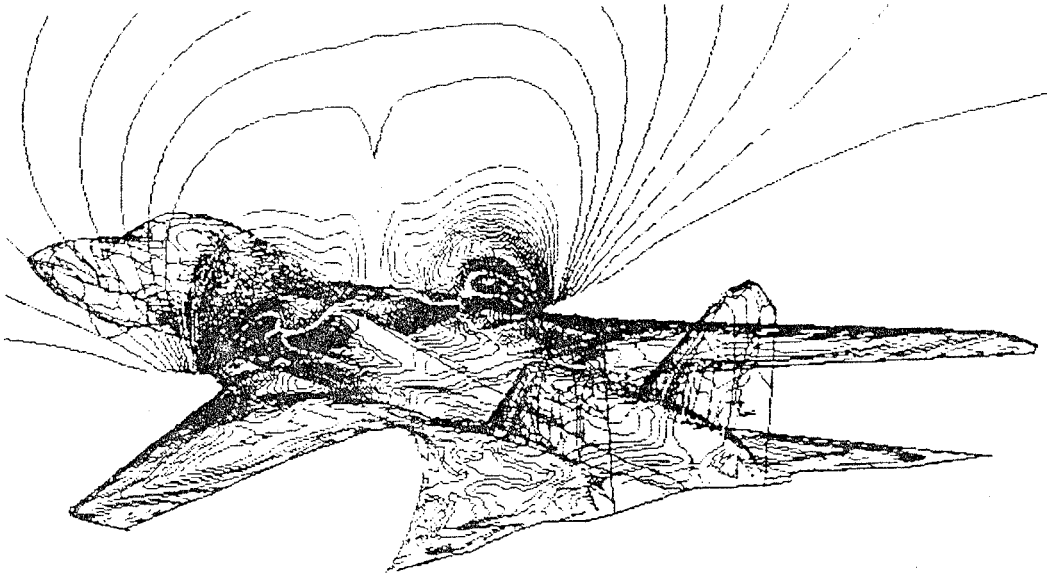


Figure 5: Isomach contours on upper wing/body surface and in a cross-sectional plane of F-14-type aircraft; $M_\infty = 0.80$, $\alpha = 20$ deg.

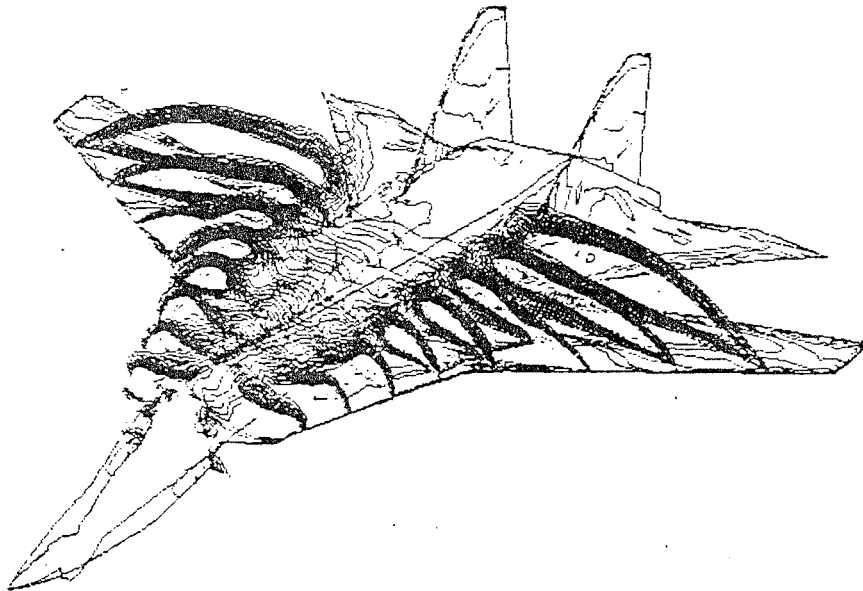


Figure 6: Entropy contours on upper wing/body surface and various cross-sectional planes of F-14-type aircraft; $M_\infty = 0.80$, $\alpha = 20$ deg.

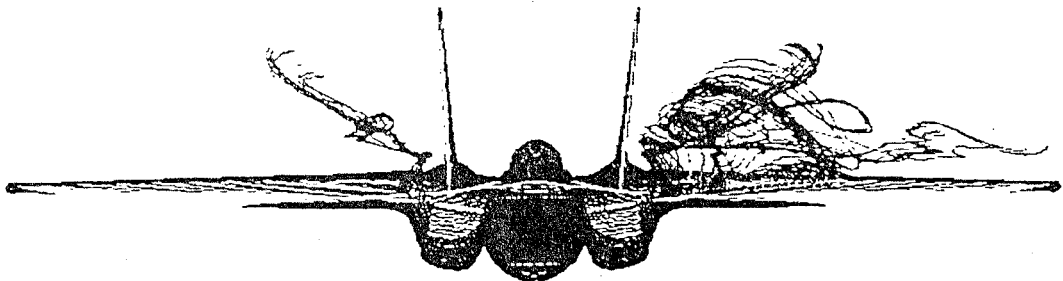


Figure 7: Streamlines from leading edge of wing and glove of F-14-type aircraft; $M_\infty = 0.80$, $\alpha = 20$ deg.; front view.

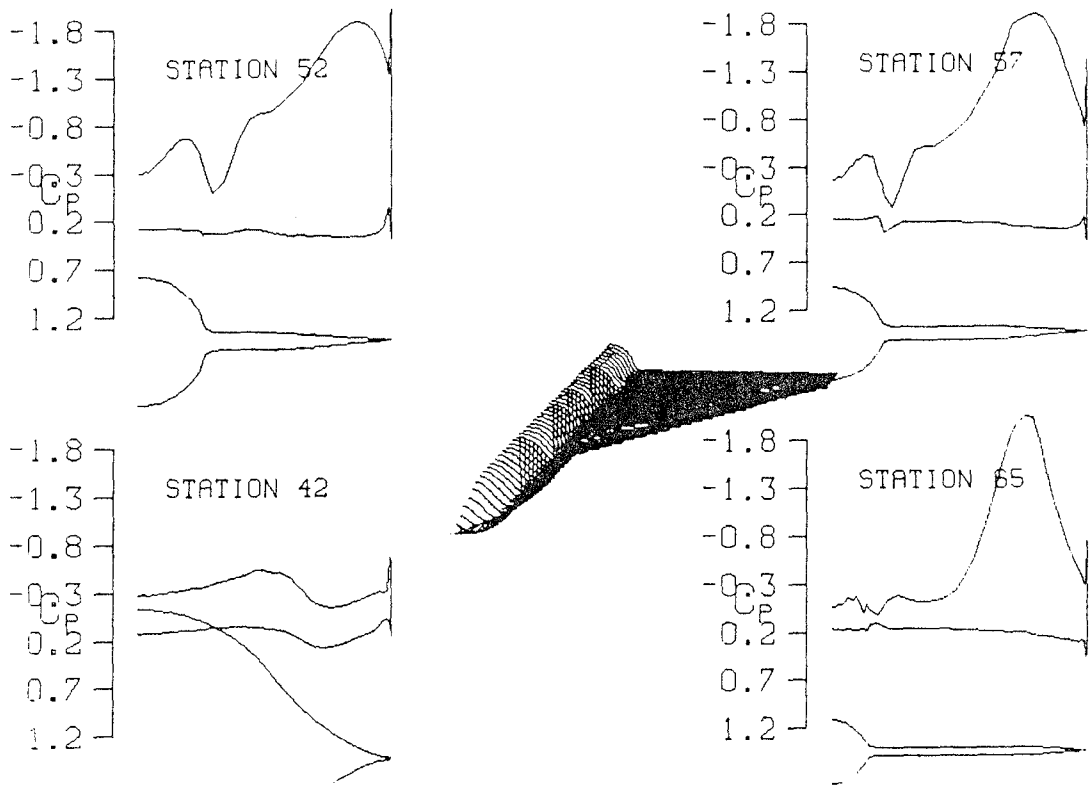


Figure 8: Computed cross-sectional surface pressure distributions on chine-forebody configuration; $M_\infty = 0.20$, $\alpha = 25$ deg.

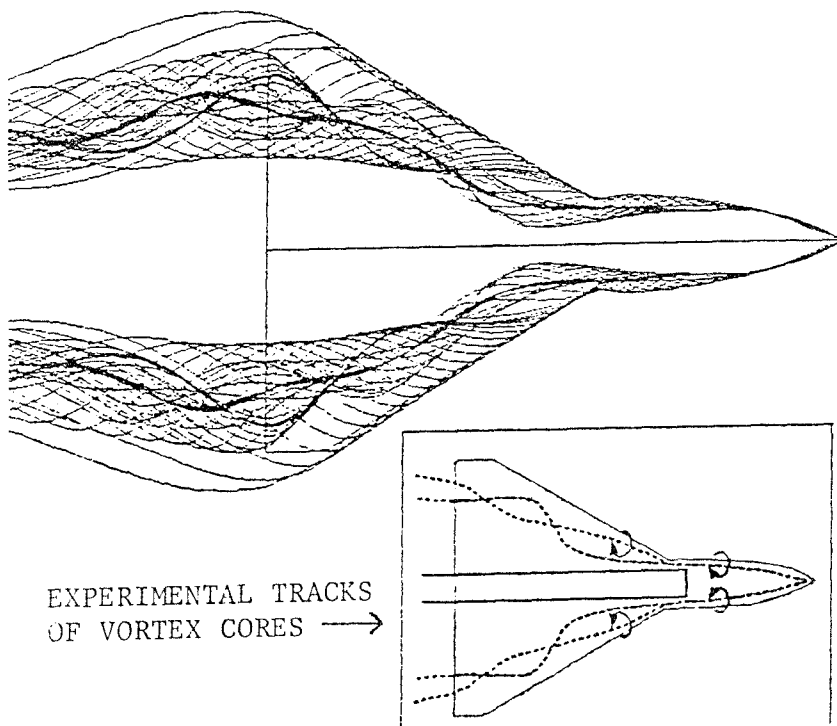


Figure 9: Top view of streamlines on chine-forebody configuration; $M_\infty = 0.20$, $\alpha = 25$ deg.; inset: experimental tracks of vortex cores (from Ref. 11).

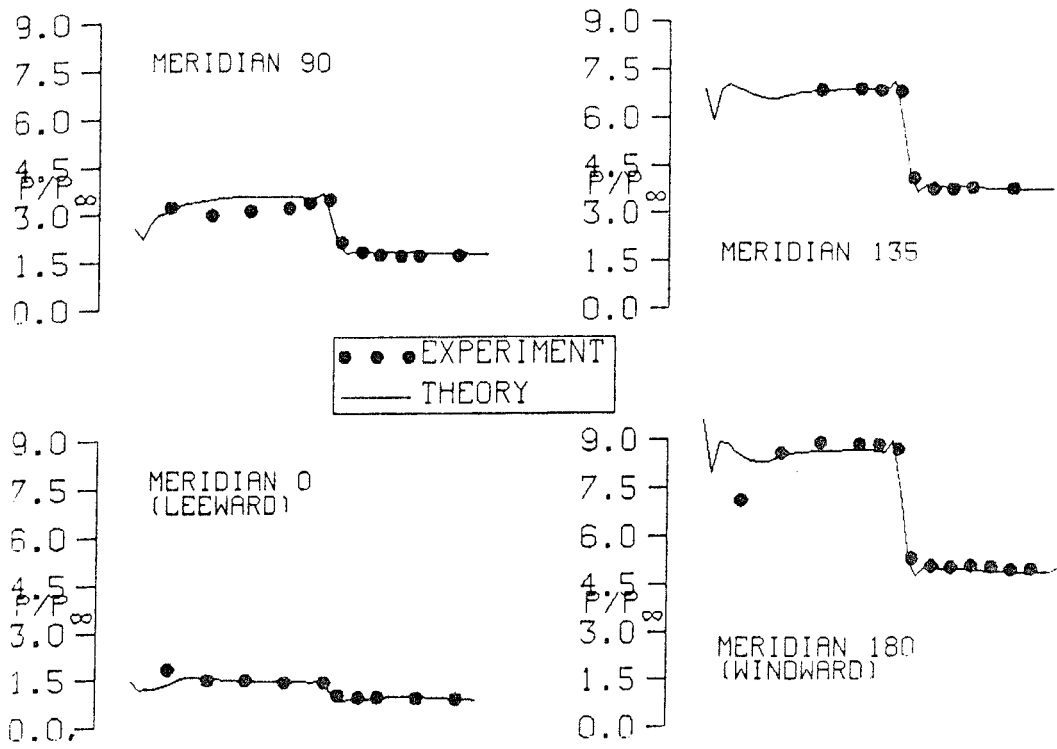


Figure 10: Longitudinal surface pressure distributions on biconic missile body; $M_\infty = 6.0$, $\alpha = 10$ deg.